Journal of Solid State Chemistry 184 (2011) 3150–3157

Contents lists available at SciVerse ScienceDirect

Journal of Solid State Chemistry

journal homepage: www.elsevier.com/locate/jssc

$Pb_{2.85}Ba_{2.15}Fe_4SnO_{13}$: A new member of the $A_nB_nO_{3n-2}$ anion-deficient perovskite-based homologous series

Oleg E. Korneychik [a], Maria Batuk [b,*], Artem M. Abakumov [b], Joke Hadermann [b], Marina G. Rozova [a], Denis V. Sheptyakov [c], Konstantin V. Pokholok [a], Dmitry S. Filimonov [a], Evgeny V. Antipov [a]

[a] Department of Chemistry, Moscow State University, 119992 Moscow, Russia
[b] Electron Microscopy for Materials Research (EMAT), University of Antwerp, Groenenborgerlaan 171, B-2020 Antwerp, Belgium
[c] Laboratory for Neutron Scattering, Paul Scherrer Institut, CH-5232 Villigen, Switzerland

ARTICLE INFO

Article history:
Received 6 July 2011
Received in revised form
12 September 2011
Accepted 22 September 2011
Available online 29 September 2011

Keywords:
Perovskite
Lone pair
Neutron powder diffraction
Mössbauer spectroscopy

ABSTRACT

$Pb_{2.85}Ba_{2.15}Fe_4SnO_{13}$, a new $n=5$ member of the anion-deficient perovskite based $A_nB_nO_{3n-2}$ (A=Pb, Ba, B=Fe, Sn) homologous series, was synthesized by the solid state method. The crystal structure of $Pb_{2.85}Ba_{2.15}Fe_4SnO_{13}$ was investigated using a combination of neutron powder diffraction, electron diffraction, high angle annular dark field scanning transmission electron microscopy and Mössbauer spectroscopy. It crystallizes in the *Ammm* space group with unit cell parameters $a=5.7990(1)$ Å, $b=4.04293(7)$ Å and $c=26.9561(5)$ Å. The $Pb_{2.85}Ba_{2.15}Fe_4SnO_{13}$ structure consists of quasi two-dimensional perovskite blocks separated by $1/2[110](\bar{1}01)_p$ crystallographic shear (CS) planes. The corner-sharing FeO_6 octahedra at the CS planes are transformed into edge-sharing FeO_5 distorted tetragonal pyramids. The octahedral positions in the perovskite blocks between the CS planes are jointly taken up by Fe and Sn, with a preference of Sn towards the position at the center of the perovskite block. The chains of FeO_5 pyramids and $(Fe,Sn)O_6$ octahedra of the perovskite blocks delimit six-sided tunnels at the CS planes occupied by double chains of Pb atoms. The compound is antiferromagnetically ordered below $T_N=368\pm15$ K.

1. Introduction

Recently the existence of a new anion-deficient perovskite-based homologous series with the general formula $A_nB_nO_{3n-2}$ was reported [1]. The $A_nB_nO_{3n-2}$ crystal structures consist of two-dimensional perovskite blocks shaped by the $(\bar{1}01)_p$ perovskite planes. The blocks can be represented as a stacking of the perovskite ABO and O_2 layers alternating along the $[10\bar{1}]_p$ direction of the parent perovskite structure. At the interface between two blocks, a single O_2 layer is missing, which results in an overall anion deficiency of the $A_nB_nO_{3n-2}$ homologues in comparison with the ABO_3 perovskite composition. The subtraction of the oxygen layer is accommodated by a displacement of the blocks relative to each other by a $1/2[110]_p$ vector. This displacement, combined with the oxygen deficiency, transforms the corner sharing BO_6 octahedra of the perovskite framework into BO_5 distorted tetragonal pyramids, edge shared into infinite chains running along the interfaces. Such interfaces can be formally considered as a result of a periodic application of the $1/2[110](\bar{1}01)_p$ crystallographic shear operation to the perovskite structure, and the interfaces are referred to as crystallographic shear (CS) planes [2–7]. The amount of ABO layers (or the number of octahedral units along $[10\bar{1}]_p$) in the perovskite blocks is defined by homologue's number n as $n-2$. The BO_6 octahedra of the perovskite blocks share corners with the BO_5 pyramids at the CS planes, together delimiting six-sided tunnels occupied by two columns of A-cations with a lone electron pair (Pb^{2+}, Bi^{3+}).

Such compounds as $Pb_{4/3}Sr_{2/3}Fe_2O_5$ [8], $Pb_{1.33}Sr_{0.67-x}Ba_xFe_2O_5$ ($0\le x\le0.67$) [9], $Pb_{2-x}Ba_xFe_2O_5$ ($0.6\le x\le1.0$) [10] and $Pb_2Mn_2O_5$ [11] represent the $n=4$ member of the $A_nB_nO_{3n-2}$ homologous series. The thickness of the perovskite block can be enlarged by a partial replacement of B^{3+} by another B cation with a formal charge of 4+ and a strong affinity towards octahedral coordination. Using Ti^{4+} for partial heterovalent replacement of Fe^{3+}, two following members of the series with the compositions $Pb_{2.9}Ba_{2.1}Fe_4TiO_{13}$ ($n=5$) and $Pb_{3.8}Bi_{0.2}Ba_2Fe_{4.2}Ti_{1.8}O_{16}$ ($n=6$) were obtained [1]. All the members of the series crystallize in an orthorhombic crystal system with lattice parameters related to the parameters of the basic perovskite structure a_p as $a\approx a_p\sqrt{2}$, $b\approx b_p$, $c\approx9.7$ Å$+(n-2)a_p\sqrt{2}$ (the first term of the sum stands for the thickness of the interface between the perovskite blocks, which is nearly constant for all members, and the second term stands for the thickness of the perovskite blocks; n is the homologue number, $a_p\approx4.06$ Å).

* Corresponding author. Fax: +32 3265 3257.
E-mail address: Maria.Batuk@ua.ac.be (M. Batuk).

0022-4596/$ - see front matter © 2011 Elsevier Inc. All rights reserved.
doi:10.1016/j.jssc.2011.09.029

In this work we applied the same strategy to obtain a new member of the $A_nB_nO_{3n-2}$ homologous series using Sn^{4+}, because tin, similar to titanium, has a stable octahedral coordination and can substitute Fe^{3+} in the perovskite blocks, maintaining the charge balance. We isolated the new $Pb_{2.85}Ba_{2.15}Fe_4SnO_{13}$ compound representing $n=5$ member of the $A_nB_nO_{3n-2}$ homologous series and determined its crystal structure and magnetic properties.

2. Experimental

The sample with the bulk composition $Pb_3Ba_2Fe_4SnO_{13}$ was synthesized by a high temperature solid state reaction between PbO, $BaCO_3$, Fe_2O_3 and SnO_2 in air. The initial components were mixed in stoichiometric amounts, ground thoroughly and pressed into 10 mm pellets. The thermal treatment included heating at 850 °C for 50 h, then at 900, 950 and 980 °C for 10 h each with intermediate regrinding.

Powder X-ray diffraction (PXD) data were collected on a Huber G670 Guinier diffractometer. Powder neutron diffraction (PND) data were collected at the high resolution powder diffractometer HRPT with the use of a radiation-type furnace for heating from room temperature to 550 K and an ILL type ^{4}He flow cryostat for cooling down to 1.5 K. The data blocks taken at $T=550$ K with the wavelengths $\lambda=1.494$ Å and 1.886 Å were simultaneously used for the Rietveld refinement. Crystal structure refinement was performed with the JANA2006 program [12].

Electron diffraction (ED) patterns were obtained with Philips CM20 and FEI Tecnai G^2 transmission electron microscopes. Energy dispersive X-ray (EDX) analysis was performed with a JEOL 5510 scanning electron microscope equipped with the Oxford INCA system. EDX spectra from 62 different crystallites were used for the determination of chemical composition. High angle annular dark field scanning transmission electron microscopy (HAADF-STEM) images were acquired using an FEI Tecnai G^2 electron microscope. The theoretical HAADF-STEM images were calculated by means of the QSTEM software [13].

Mössbauer spectroscopy (^{57}Fe and ^{119}Sn) was performed on samples enriched with ^{57}Fe (50%) and ^{119}Sn (100%) in transmission mode using a constant acceleration Mössbauer spectrometer (MS1104, Rostov-na-Donu, Russia) with ^{57}Co/Rh and $Ba^{119}SnO_3$ γ-ray sources. Velocities were calibrated with standard α-Fe or sodium nitroprusside absorbers, isomer shifts were related to α-Fe or $BaSnO_3$. Spectra treatment was performed using "UnivemMS" [14] and custom software.

3. Results and discussion

3.1. Preliminary characterization

According to the EDX analysis, the composition of the studied compound corresponds to the formula $Pb_{2.85(8)}Ba_{2.15(7)}Fe_{4.01(9)}Sn_{1.02(8)}O_{13}$ and will be denoted hereafter as $Pb_{2.85}Ba_{2.15}Fe_4SnO_{13}$. The difference between proposed and derived compositions can be explained by the presence of the numerous stacking faults in the sample (see below). The ED patterns of $Pb_{2.85}Ba_{2.15}Fe_4SnO_{13}$ were indexed in an orthorhombic crystal system with the lattice parameters: $a \approx 5.8$ Å $\approx a_p\sqrt{2}$; $b \approx 4.0$ Å $\approx a_p$; $c \approx 27$ Å $\approx 5a_p\sqrt{2}$ (a_p—the parameter of the perovskite subcell) (Fig. 1). The only reflection condition derived from the ED patterns is *hkl:* $k+l=2n$, reflecting the *A*-centering and compatible with the space groups *A*222, *A*2*mm* (*Am*2*m*, *Amm*2) and *Ammm* or their monoclinic subgroups. Using the ED data, the room temperature PXD and PND patterns were indexed, providing the unit cell parameters $a=5.7740(1)$ Å, $b=4.0231(1)$ Å and $c=26.8682(6)$ Å.

The PND patterns collected at temperatures lower than 350 K contain a set of extra reflections, which do not fit the positions defined by the proposed *A*-centered orthorhombic unit cell (Fig. 2). These reflections originate from magnetic ordering, because the ED study down to liquid nitrogen temperature does not reveal any of these extra reflections. The intensity of these reflections on the PND patterns increases monotonically with decreasing temperature. The whole set of magnetic diffraction peaks can be indexed with the propagation vector $\mathbf{k}=[0\ 1/2\ 1/2]$, indicating long-range antiferromagnetic (AFM) ordering. The intensity ratio of the magnetic $(1\ 1/2\ 1/2)_m$ and nuclear 104 reflections is plotted against T in Fig. 3. The Neel temperature can be estimated from the empirical formula $I=I_0[1-(T/T_N)^\alpha]^\beta$, with four adjustable parameters: I_0 is the intensity ratio of the magnetic and nuclear peaks at $T=0$ K; T_N — the Neel temperature; and α and β are the exponential parameters. The fit, which is shown as a solid line in Fig. 3, yields the antiferromagnetic transition temperature $T_N=368\pm15$ K ($\alpha=1.9\pm0.3$, $\beta=0.9\pm0.2$).

3.2. Structure solution and refinement

The crystal structure of $Pb_{2.85}Ba_{2.15}Fe_4SnO_{13}$ was solved from PND data taken at $T=550$ K, above the Neel temperature. The lattice parameters and the intensity distribution on the PXD and PND patterns reflect that $Pb_{2.85}Ba_{2.15}Fe_4SnO_{13}$ possesses a structure close to that of the $Pb_{2.9}Ba_{2.1}Fe_4TiO_{13}$ phase [1]. Thus, the atomic coordinates of the $Pb_{2.9}Ba_{2.1}Fe_4TiO_{13}$ crystal structure were taken as an initial model. The refinement was carried out in the most symmetric *Ammm* space group. The possibility of monoclinic distortion and the lowering of the symmetry from orthorhombic to a monoclinic *A*2/*m* space group was tested in the refinement too, but no significant improvement of the refinement quality was observed. The overall cation composition was fixed according to the EDX result. In spite of different scattering lengths of Pb, Ba, Fe and Sn (9.405, 5.07, 9.45 and 6.225 fm, respectively), the refinement of the occupancy factors of four crystallographic positions PbBa1, PbBa2, FeSn1 and FeSn2 from solely PND data was not reliable. The occupancy factors were refined from room temperature PND data (excluding the magnetic contribution)

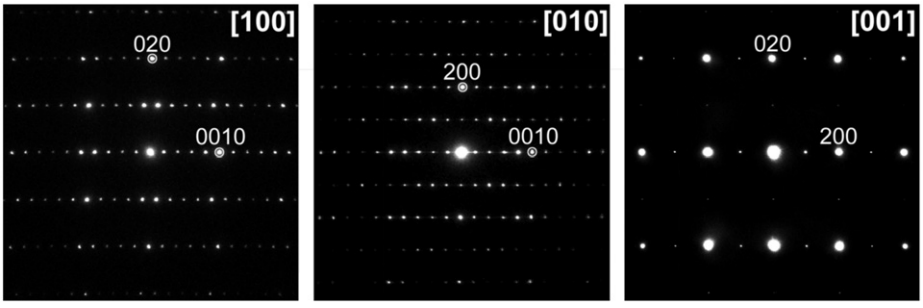

Fig. 1. Electron diffraction patterns of $Pb_{2.85}Ba_{2.15}Fe_4SnO_{13}$ along the [100], [010] and [001] directions.

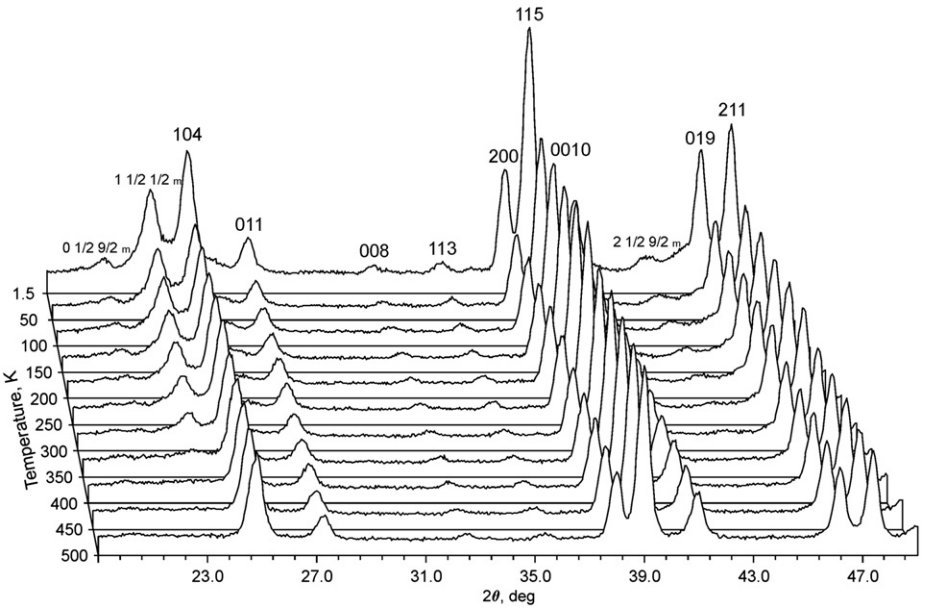

Fig. 2. PND patterns of $Pb_{2.85}Ba_{2.15}Fe_4SnO_{13}$ collected in the 1.5–500 K temperature range. $(0\ 1/2\ 9/2)_m$, $(1\ 1/2\ 1/2)_m$ and $(2\ 1/2\ 9/2)_m$ reflections are attributed to the magnetic structure.

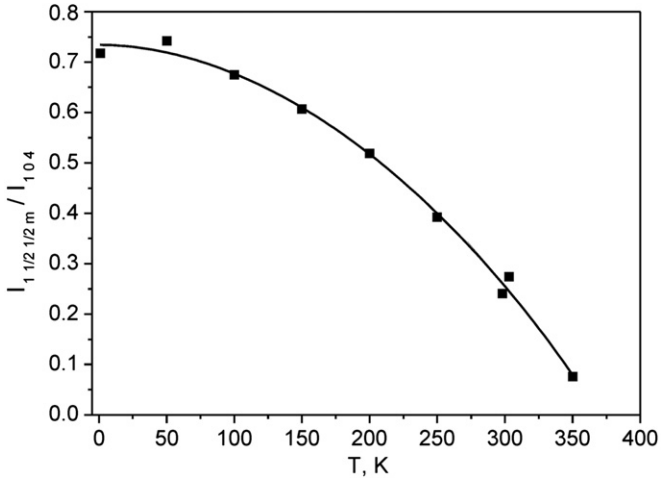

Fig. 3. Temperature dependence of the intensity ratio of the magnetic $(1\ 1/2\ 1/2)_m$ reflection to nuclear 104 reflection. The solid line is a fitting curve.

combined with the PXD data. The obtained occupancies were then used for the final refinement against the PND data at $T=550$ K. According to Mössbauer spectroscopy data, the formal oxidation state for the iron atoms is +3, for the tin atoms the oxidation state is +4, therefore no anion deficiency is present in this compound, and the occupancies of the oxygen positions were not refined. The refinement of the anisotropic atomic displacement parameter for the O4 atom revealed a significant U_{11} component, and this atom was displaced along the a axis from the 4-fold to the 8-fold position with halved occupancy. The final refinement was performed with an isotropic approximation for the atomic displacement parameters. Close inspection of the difference PND curve after refinement revealed that an admixture phase is present in the sample. It was identified as the next $n=6$ member of the $A_nB_nO_{3n-2}$ homologous series with an orthorhombic unit cell, the lattice parameters $a=5.799(1)$ Å, $b=4.0553(6)$ Å, $c=32.695(5)$ Å, space group *Imma* and the tentative composition $Pb_4Ba_2Fe_4Sn_2O_{16}$. The admixture phase was included into the refinement adopting the atomic coordinates of the $Pb_{3.8}Bi_{0.2}Ba_2Fe_{4.2}Ti_{1.8}O_{16}$ crystal structure [1]. The amount of the $n=6$ phase was refined to 14.5(3) wt%. This number has to be treated with care, however, because of significant overlap of the reflections of the $n=5$ and $n=6$ phases. Although the crystals with the $n=6$ structure were not observed, a lot of planar defects (intergrowths of $n=5$ and $n=6$ crystals, insertion of $n=6$ lamellae into the matrix of $n=5$) can be seen on HAADF-STEM images (see below). Introducing the second phase improves the fit, reducing R_P from 0.043 to 0.038. The experimental, calculated and difference PND profiles after the Rietveld refinement are shown in Fig. 4. The crystallographic parameters for $Pb_{2.85}Ba_{2.15}Fe_4SnO_{13}$ are given in Tables 1 and 2; the main interatomic distances are listed in Table 3.

The crystal structure of $Pb_{2.85}Ba_{2.15}Fe_4SnO_{13}$ consists of a framework of BO_6 and BO_5 polyhedra (Fig. 5a). Corner sharing BO_6 octahedra form quasi two-dimensional perovskite blocks separated by the chains of edge-sharing BO_5 distorted tetragonal pyramids. The m_x mirror plane of the *Ammm* space group passes through the chain of the BO_5 pyramids splitting the O4 position forming the common edges of the pyramids. From two O4 atoms on both sides of the m_x plane only one is physically present in the structure because of the halved occupancy of this position. One can suggest the most probable atomic arrangement, where the m_x plane is not a symmetry operation of the chain, but two chains with mirror-related configurations are randomly distributed in the structure (Fig. 5b). These chains, arbitrarily called "left" (L) and "right" (R), differ only by the direction of the sideways displacement along the a axis of the O4 atoms. Disordered L and R pyramidal chains are also present in the high temperature *Imma* structure of the $n=4$ $Pb_{2-x}Ba_xFe_2O_5$ member [10]. In that compound, the ordering of the chains is established at the second order phase transition into the low temperature *Pnma* structure, where either L or R chains occur within the same layer and the L and R layers alternate along the c axis. One can assume that such intralayer ordering remains in the $Pb_{2.85}Ba_{2.15}Fe_4SnO_{13}$ structure, but that the interlayer ordering is lost. The interlayer disorder then can be described as a random occurrence of two stacking types of the layers of the pyramidal chains, corresponding to either an -R-L-R-L- or an -L-L-L-L- sequence along the c axis (Fig. 6). Such local configurations can be obtained from the parent

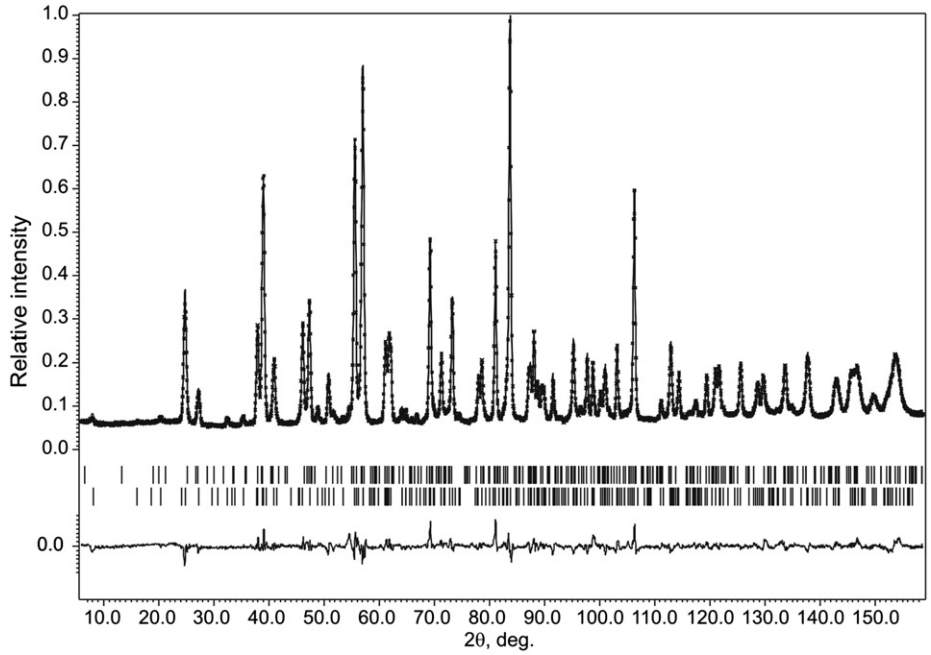

Fig. 4. Experimental, calculated and difference PND profiles after the Rietveld refinement ($\lambda=1.886$ Å, $T=550$ K). The upper row of tick marks denotes the reflection positions for the $Pb_4Ba_2Fe_4Sn_2O_{16}$ admixture phase and the lower row of tick marks denotes the reflection positions for the $Pb_{2.85}Ba_{2.15}Fe_4SnO_{13}$ phase.

Table 1
Selected parameters from Rietveld refinement for $Pb_{2.85}Ba_{2.15}Fe_4SnO_{13}$.

Formula	$Pb_{2.85}Ba_{2.15}Fe_4SnO_{13}$
Space group	*Ammm*
a (Å)	5.7990(1)
b (Å)	4.04293(7)
c (Å)	26.9561(5)
Z	2
Cell volume (Å^3)	631.99(2)
Calculated density (g/cm^3)	7.543(4)
T (K)	550
Radiation	Neutrons:
	Block I: $\lambda=1.886$ Å
	Block II: $\lambda=1.494$ Å
Parameters refined	24
R_F (block I), R_F (block II)	0.027, 0.026
R_P, R_{wP}	0.038, 0.049

Table 2
Positional and atomic displacement parameters for $Pb_{2.85}Ba_{2.15}Fe_4SnO_{13}$ at $T=550$ K.

Atom	Position	Occupancy	*x/a*	*y/b*	*z/c*	U_{iso} (Å^2)
Pb1	4*j*	1	1/2	1/2	0.3052(1)	0.026(1)
BaPb1	4*i*	0.72Ba+0.28Pb	0	0	0.1000(2)	0.022(1)
BaPb2	2*d*	0.72Ba+0.28Pb	1/2	1/2	1/2	0.028(2)
Fe1	4*i*	1	0	0	0.2933(1)	0.008(1)
FeSn1	4*j*	0.8Fe+0.2Sn	1/2	0	0.3958(1)	0.007(1)
FeSn2	2*b*	0.4Fe+0.6Sn	0	0	1/2	0.002(1)
O1	4*j*	1	1/2	1/2	0.3873(2)	0.018(1)
O2	8*n*	1	0.2486(10)	0	0.4456(2)	0.013(1)
O3	8*n*	1	0.2626(5)	0	0.3344(1)	0.013(1)
O4	8*n*	0.5	0.0294(9)	0	0.2190(1)	0.005(1)
O5	2*a*	1	0	1/2	1/2	0.002(1)

Ammm disordered structure by decreasing the symmetry down to the *Pnmm* and *A*12/*m*1 subgroups, respectively.

The cation positions in the BO_5 tetragonal pyramids are occupied exclusively by the Fe^{3+} cations (Fe1 cations). Bond valence sum (BVS) was calculated for this position. According to Brown et al., the R_0 constant in the BVS equation as estimated from the room temperature bond lengths cannot be directly used for calculating BVS at higher temperatures [15,16]. The $R_0(T)$ value as a function of temperature can be calculated as $R_0(T)=R_0+(dR/dT)\Delta T$, where dR/dT is a function of the bond valence *s* and ΔT is the temperature increase with respect to room temperature. For the Fe^{3+}–O bond at $T=550$ K, $dR/dT\approx 2\cdot 10^{-5}$ Å K^{-1} (see Fig. 5 in Ref. [16]), giving the corrected BVS of 2.88, in good agreement with the nominal valence of +3.

Table 3
Selected interatomic distances for $Pb_{2.85}Ba_{2.15}Fe_4SnO_{13}$ (Å) at $T=550$ K.

Pb1–O1	2.212(6) × 1	Fe1–O3	1.884(3) × 2
Pb1–O3	2.570(2) × 4	Fe1–O4	2.010(5) × 1
Pb1–O4	2.806(5) × 1	Fe1–O4	2.0554(9) × 2
BaPb1–O1	2.9197(8) × 2	FeSn1–O1	2.0345(7) × 2
BaPb1–O2	2.771(4) × 4	FeSn1–O2	1.982(5) × 2
BaPb1–O3	3.086(3) × 4	FeSn1–O3	2.152(4) × 2
BaPb1–O5	2.696(5) × 1	FeSn2–O2	2.056(5) × 4
BaPb2–O1	3.039(5) × 2	FeSn2–O5	2.0215(1) × 2
BaPb2–O2	2.892(4) × 8		
BaPb2–O5	2.8995(1) × 2		

The Fe^{3+} and Sn^{4+} cations are intermixed at the BO_6 octahedral sites in such a way that the octahedra in the interior part of the perovskite block contain more tin (the FeSn2 position) than the octahedra at the periphery of the perovskite block (the FeSn1 position). The BO_6 octahedra are only weakly deformed, but the position of the cations inside the octahedra is drastically different for the $(FeSn1)O_6$ and $(FeSn2)O_6$ octahedra. The FeSn2 cations are situated almost at the center of the octahedron (d(FeSn2)–O2 = 2.06 Å, d(FeSn2)–O5 = 2.02 Å), while the FeSn1 cations are strongly displaced towards the O2-O2 edge (d(FeSn1) – O3 = 2.15 Å; d(FeSn1) – O2 = 1.98 Å). This displacement is caused by an electrostatic repulsion due to a short FeSn1—Pb1 contact. As already stated, the distribution of Fe and Sn over the FeSn1 and FeSn2 positions is not completely random: the Sn^{4+} cations preferentially occupy the FeSn2 position at the center of

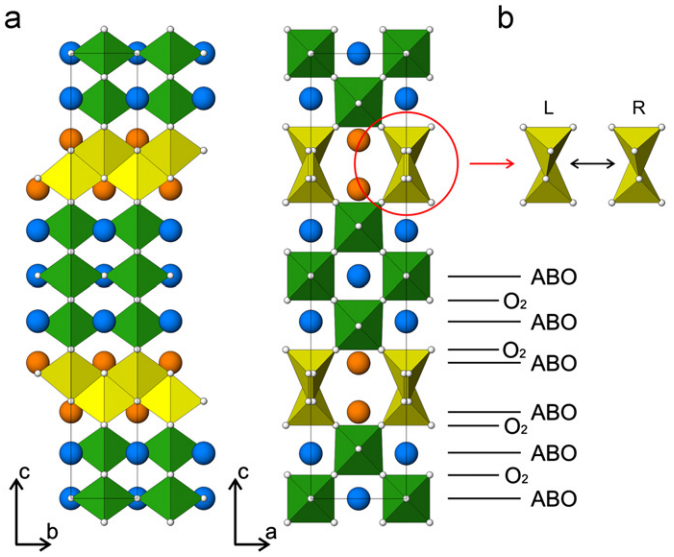

Fig. 5. (a) Crystal structure of $Pb_{2.85}Ba_{2.15}Fe_4SnO_{13}$ viewed along the [100] and [010] zone axes. Yellow distorted tetragonal pyramids are occupied exclusively by Fe cations, the Pb cations in the six-sided tunnels are shown as orange spheres. The green octahedra are centered jointly by Fe and Sn cations. Pb exclusively occupy the six-sided tunnels. The rest of the lead and all barrium atoms are situated in the perovskite blocks (they are shown as big spheres). The Pb and Ba atoms in the perovskite blocks are shown as large blue spheres. Oxygen atoms are shown as small grey spheres. (b) Two mirror-related configurations of the double chains of FeO_5 tetragonal pyramids occurring in the structure in a disordered manner. (For interpretation of the references to color in this figure legend, the reader is referred to the web version of this article.)

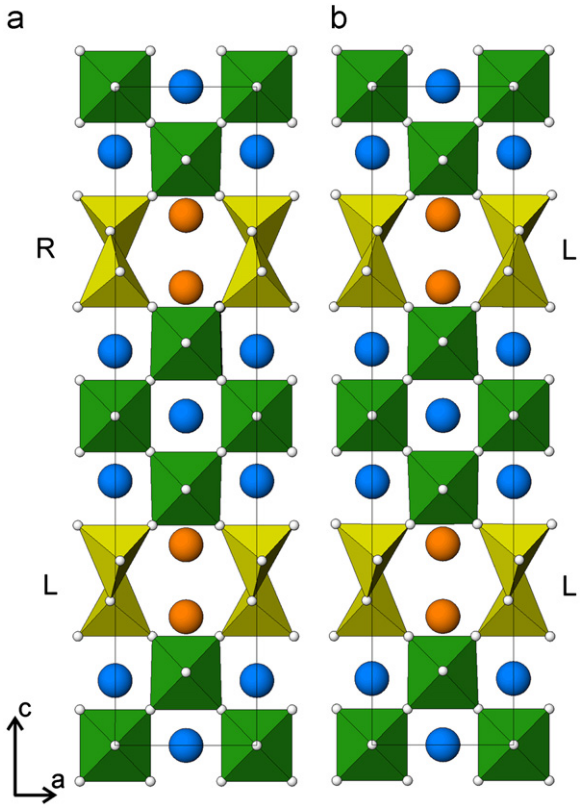

Fig. 6. The local -R-L-R-L- or -L-L-L-L- stacking sequences of the pyramidal chains, represented as the structure models with the (a) *Pnmm* and (b) *A*12/*m*1 subgroups of the *Ammm* space group of the parent disordered $Pb_{2.85}Ba_{2.15}Fe_4SnO_{13}$ structure.

the perovskite block. Presumably, this allows to maintain local electroneutrality, since only divalent cations are located at the A positions. This cation distribution is clearly visible on the HAADF-STEM images (see below).

The tetragonal pyramidal chains are connected to the octahedra of the perovskite blocks through common corners, together delimiting six-sided tunnels, exclusively filled with double chains of Pb^{2+} cations. The coordination environment of the Pb1 cations is very asymmetric with a shortest Pb1–O1 distance of 2.21 Å and a longest Pb1–O4 distance of 2.81 Å. The short Pb–O bond reflects a high degree of covalency, related to mixing of Pb 6*s* and O 2*p* states and the spatial localization of the lone electron pairs [17,18]. Indeed, such localization was demonstrated previously in the $n=4$ $Pb_{2-x}Ba_xFe_2O_5$ member by topologic analysis of the electron localization function [10]. The rest of the Pb atoms are intermixed with Ba at the A positions of the perovskite blocks.

Close compositions of the A-sublattice and the identical temperatures of the PND measurements (550 K) make possible a direct comparison of the $Pb_{2.9}Ba_{2.1}Fe_4TiO_{13}$ [1] and $Pb_{2.85}Ba_{2.15}Fe_4SnO_{13}$ structures. The structures are very similar in the distribution of the Pb and Ba cations over the A-positions and the Fe and Ti(Sn) cations over the B-positions. The only noticeable changes are related to difference in ionic radii of Ti^{4+} (0.605 Å) and Sn^{4+} (0.690 Å). Larger ionic radius of Sn^{4+} leads to slight enlargement of all lattice parameters and increases the unit cell volume from 622 $Å^3$ for $Pb_{2.9}Ba_{2.1}Fe_4TiO_{13}$ to 632 $Å^3$ for $Pb_{2.85}Ba_{2.15}Fe_4SnO_{13}$. Average interatomic distance for the octahedrally coordinated Fe*M*1 and Fe*M*2 (*M*=Ti, Sn) positions increases concomitantly with the fraction of the M cations. The Fe*M*1 position, preferentially occupied by the Fe cations, demonstrates an increase of the average Fe*M*1–O distance by 0.3% only by replacing Ti by Sn. Such increase for the Fe*M*2 position, preferentially occupied by the M cations, is significantly larger (1.7%). This indirectly confirms the correctness of the B-cation distribution in both structures. Minor structure changes do not noticeably affect the magnetic properties: both compounds are antiferromagnets with close Néel temperatures of $T_N=368$ K for *M*=Sn and 407 K for *M*=Ti [1].

3.3. HAADF-STEM imaging

HAADF-STEM images give information on the cation positions as the intensity of the atoms on the image is proportional to Z^n ($1<n<2$), where *Z* is the atomic number. Fig. 7a and b shows HAADF-STEM images of $Pb_{2.85}Ba_{2.15}Fe_4SnO_{13}$ along the [010] and [100] directions, respectively. The images show the long range ordered sequence of the perovskite blocks with uniform thickness. On the [010] HAADF-STEM image the brightest pairs of dots correspond to the Pb pairs ($Z_{Pb}=82$), which are situated in the six-sided tunnels formed by Fe atoms seen as very weak dots ($Z_{Fe}=26$). The dots corresponding to projections of the FeSn2–O columns in the interior part of the perovskite blocks are brighter than the dots corresponding to the FeSn1–O columns at the periphery, which confirm the distribution of Fe and Sn cations among these positions obtained from the Rietveld refinement. Both the [010] and [100] HAADF-STEM images are in good agreement with the HAADF-STEM images calculated using the structural parameters obtained from the Rietveld refinement (Table 2).

Numerous planar defects were observed in the sample. Fig. 8a shows intergrowth of domains of the $n=5$ and $n=6$ members. Randomly distributed separate lamellae of the $n=6$ member in the matrix of the $n=5$ structure are represented in Fig. 8b and Fig. S1 of the Supporting Information. Lamellae of the $n=4$ member were also observed (see Fig. S2 of the Supporting Information). Separate crystals with the $n=6$ structure were not observed.

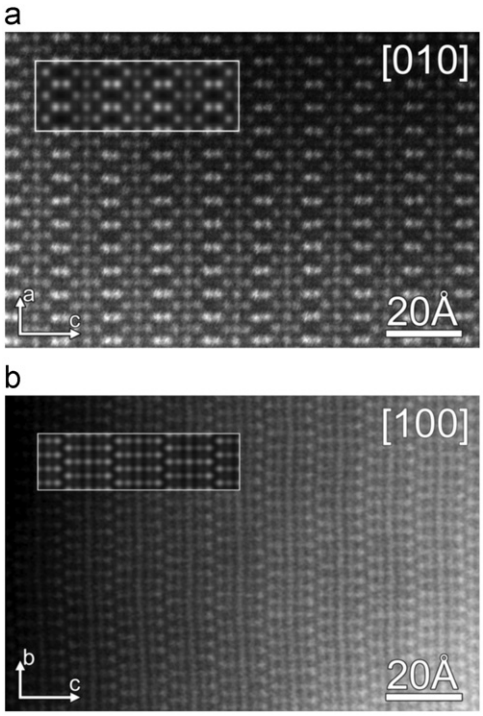

Fig. 7. HAADF-STEM images of $Pb_{2.85}Ba_{2.15}Fe_4SnO_{13}$ along the [010] (a) and [100] (b) zone axis. The calculated images are inserted (outlined with a white rectangle).

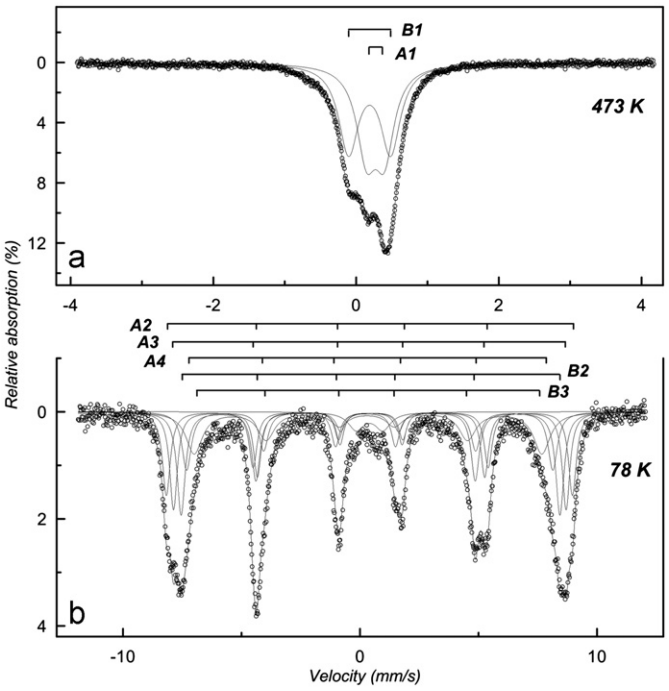

Fig. 9. ^{57}Fe Mossbauer spectra of $Pb_{2.85}Ba_{2.15}Fe_4SnO_{13}$ recorded at 473 K (a) and 78 K(b).

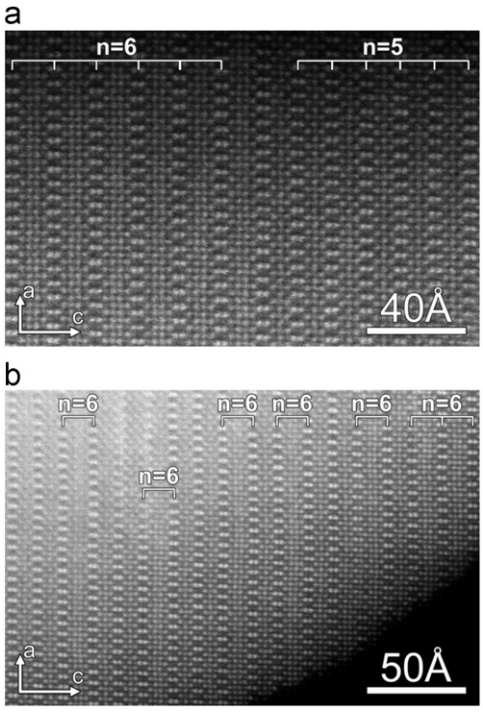

Fig. 8. (a) [010] HAADF-STEM image of the intergrowth of the $n=5$ and $n=6$ structures and (b) [010] HAADF-STEM image of the $n=5$ showing random insertion of the lamellas of the $n=6$ member.

3.4. Mössbauer spectroscopy

$Pb_{2.85}Ba_{2.15}Fe_4SnO_{13}$ was characterized by ^{57}Fe and ^{119}Sn Mössbauer spectroscopy at temperatures above and below the magnetic phase transitions, 473 K and 78 K respectively. The ^{57}Fe spectrum taken in the paramagnetic region at 473 K is shown in Fig. 9a. It is composed of two paramagnetic doublets A1 and B1 of near equal areas and slightly different isomer shifts (ISs) (Table 4). According to their IS values, both doublets correspond to the Fe^{3+} cations [19]. The A1 doublet with higher IS and smaller quadrupole splitting (QS) is attributed to the octahedral crystallographic positions, while the B1 doublet—to the five-fold coordinated positions. The observed ~1:1 ratio of doublet areas supports equal occupancy of the octahedral and five-fold coordinated sites by Fe^{3+} cations, as it follows from the Rietveld refinement (Table 2).

The ^{57}Fe spectrum measured below the Neel temperature is shown in Fig. 9b and can be fitted with a number of overlapped broadened Zeeman sextets. It appears to be very similar to the Mössbauer spectra of the isostructural $Pb_{2.9}Ba_{2.1}Fe_4TiO_{13}$ and $Pb_{3.8}Bi_{0.2}Ba_2Fe_{4.2}Ti_{1.8}O_{16}$ compounds [1]. According to the hyperfine parameters, they can be divided in two groups (Table 4): group A – with higher IS's of about 0.42 mm/s – is to be attributed to the octahedral sites, and group B with IS's of about 0.32 mm/s – to five-fold coordinated sites. The sum contribution of "A" and "B" sets is nearly equal, but because of the overlapping of sextets, this is only estimation. Thus, each type of sites is represented in the spectrum by sets of sextets with various values of magnetic hyperfine fields, H_{hf}'s, caused by the presence of diamagnetic Sn^{4+} cations in nearest neighbourhood of Fe^{3+} cations reducing the H_{hf} at the ^{57}Fe nuclei. Note that the line broadening, along with the above-mentioned reason, can also imply some degree of relaxation (see below).

The ^{119}Sn Mössbauer spectrum at 473 K shows a single, slightly broadened doublet with IS=0 mm/s corresponding to Sn^{4+} cations (Fig. 10a). This agrees well with the PND refinement data suggesting the presence of tin only in the perovskite layers. Some QS and line broadening reflect a distortion of the oxygen octahedra and variations in the near neighbour charges, viz. Fe^{3+} and Sn^{4+}.

At 78 K, the spectrum could be best fitted with a broad hyperfine magnetic field distribution up to about 40 T (84% of the area) and a broadened doublet with QS similar to one appearing in the spectrum recorded at 473 K (Fig. 10b, Table 4). The appearance of magnetic

Table 4
The ^{57}Fe and ^{119}Sn Mossbauer hyperfine parameters of $Pb_{2.85}Ba_{2.15}Fe_4SnO_{13}$: IS, isomer shift relative to α-Fe or $BaSnO_3$ respectively; Δ, quadrupole splitting; ε, apparent quadrupole shift; Γ, line-width; I, relative area.

Absorber	T (K)	Component	IS (mm/s ± 0.03)	Δ (mm/s ± 0.03)	2ε (mm/s ± 0.03)	H_{hf} (T ± 0.5)	Γ (mm/s ± 0.03)	I (% ± 2)
^{57}Fe	473	A1	0.27	0.25			0.33	48
		B1	0.19	0.59			0.33	52
	78	A2	0.42		−0.05	53.2	0.4	18
		A3	0.44		−0.05	51.5	0.38	21
		A4	0.41		0	48.0	0.47	15
		B2	0.34		0.21	49.6	0.42	24
		B3	0.31		0.05	45.6	0.84	19
		D1	0.4	1.1			0.8	3
^{119}Sn	473	C1	0	0.26			1.4	100
	78	C2	0.05	0.27			1.83	16
		Dist1	0.05		0	〈50–400〉		84

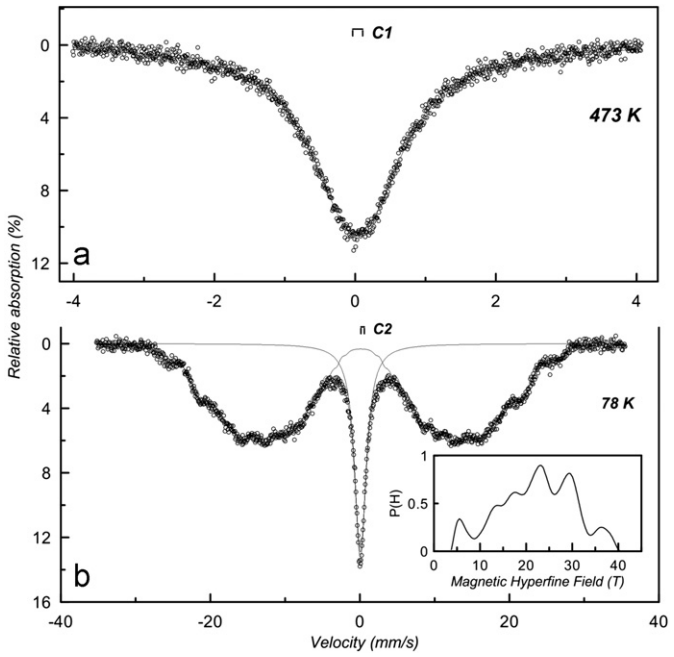

Fig. 10. ^{119}Sn Mossbauer spectra of $Pb_{2.85}Ba_{2.15}Fe_4SnO_{13}$ recorded at 473 K (a) and 78 K(b) (inset shows the corresponding magnetic field distribution).

Zeeman splitting in the ^{119}Sn Mössbauer spectrum is caused by spin polarization of diamagnetic Sn^{4+} cations by magnetic Fe^{3+} neighbours along the Fe–O–Sn chains. Consequently, the ^{119}Sn spectra are rather sensitive to the number of iron neighbours and, as it was shown for Fe- and Sn-containing perovskites and related compounds, to the geometry of the exchange paths [20,21]. As follows from the spectrum, some magnetic components (∼4–5%) are characterized by H_{hf} values of ca. 38 T. This is the highest H_{hf} value observed at ^{119}Sn nuclei so far and could be assigned to the Sn^{4+} cations located at the FeSn2 sites with all six Fe–O–Sn bond angles close to 180°, surrounded by six Fe^{3+} cations. Nevertheless, the contribution of the magnetic component with high H_{hf} is lower, and the contribution of the magnetic component with small H_{hf} is higher than it is expected from the statistical distribution of the Fe^{3+} and Sn^{4+} cations over all octahedral sites. Besides, there is a broad diamagnetic doublet of ca. 16% in the spectrum. Even though the presence of some minor impurity non-magnetic phase could not be completely ruled out, it seems unlikely that it makes the major contribution to the diamagnetic doublet in the Mössbauer spectrum. Taking into account the high content of diamagnetic Sn^{4+} cations along with the relatively high temperature of the measurements and the line broadening in the ^{57}Fe spectrum, the appearance of the strong diamagnetic doublet and the high contribution of small H_{hf}'s could be explained by a spin relaxation of Fe^{3+} in the magnetically diluted perovskite layers, partially cancelling the transferred hyperfine interaction. Similar behavior was observed in some magnetically diluted Fe and Sn containing perovskite and spinel compounds [21,22]. The ^{119}Sn spectrum is more sensitive to relaxation because the Sn^{4+} cations have no intrinsic spin moment [21].

4. Conclusion

The anion-deficient perovskite based $A_nB_nO_{3n-2}$ homologous series is expanded by the new $n=5$ member $Pb_{2.85}Ba_{2.15}Fe_4SnO_{13}$. The crystal structure of $Pb_{2.85}Ba_{2.15}Fe_4SnO_{13}$ can be represented as a result of slicing the perovskite structure by periodically arranged $1/2[110](\bar{1}01)_p$ crystallographic shear (CS) planes resulting in oxygen deficiency in comparison with the ABO_3 perovskite composition. At the CS planes, the corner-sharing BO_6 octahedra are transformed into edge-sharing distorted BO_5 distorted tetragonal pyramids. These pyramids are occupied exclusively by the Fe^{3+} cations and the A positions at the CS planes are occupied by the Pb^{2+} cations only. Mixed occupation of the A and B positions in the perovskite blocks by Pb/Ba and Fe/Sn, respectively, is realized, but with a clear preference of Sn towards the position at the center of the perovskite block. In spite of diluting the magnetic Fe^{3+} cations by non-magnetic Sn^{4+} and a high degree of cation disorder, $Pb_{2.85}Ba_{2.15}Fe_4SnO_{13}$ orders antiferromagnetically with a relatively high Neel temperature of ∼368 K.

Acknowledgments

This work was supported by Russian Foundation of Basic Research (RFBR Grants 11-03-01257-a). J.H., A.M.A. and G.V.T. acknowledge financial support from the European Union under the Framework 6 program under a contract for an Integrated Infrastructure Initiative, Reference 026019 ESTEEM. This work is partly based on experiments performed at the Swiss spallation neutron source SINQ, Paul Scherrer Institute, Villigen, Switzerland. M.B. and J.H. acknowledge financial support from the Research Foundation—Flanders (FWO G.0184.09N).

Appendix A. Supplementary material

Supplementary data associated with this article can be found in the online version at doi:10.1016/j.jssc.2011.09.029.

References

[1] A.M. Abakumov, J. Hadermann, M. Batuk, H. D'Hondt, O. Tyablikov, M.G. Rozova, K.V. Pokholok, D.S. Filimonov, D.V. Sheptyakov, A.A. Tsirlin, D. Niermann, J. Hemberger, G. Van Tendeloo, E.V. Antipov, Inorg. Chem. 49 (2010) 9508–9516.
[2] A.M. Abakumov, J. Hadermann, S. Bals, I.V. Nikolaev, E.V. Antipov, G. Van Tendeloo, Angew. Chem. (Int. Ed.) 45 (2006) 6697–6700.
[3] C. Bougerol, M.F. Gorius, I.E. Grey, J. Solid State Chem. 169 (2002) 131–138.
[4] A.M. Abakumov, J. Hadermann, G. Van Tendeloo, E.V. Antipov, J. Am. Ceram. Soc. 91 (2008) 1807–1813.
[5] C. Lepoittevin, J. Hadermann, S. Malo, O. Perez, G. Van Tendeloo, M. Hervieu, Inorg. Chem. 48 (2009) 8257–8262.
[6] S. Malo, C. Lepoittevin, O. Perez, S. Hebert, G. Van Tendeloo, M. Hervieu, Chem. Mater. 22 (2010) 1788–1797.
[7] A.M. Abakumov, D. Batuk, J. Hadermann, M.G. Rozova, D.V. Sheptyakov, A.A. Tsirlin, D. Niermann, F. Waschkowski, J. Hemberger, G. Van Tendeloo, E.V. Antipov, Chem. Mater. 23 (2011) 255–265.
[8] V. Raynova-Schwarten, W. Massa, D. Babel, Z. Anorg. Allg. Chem. 623 (1997) 1048–1054.
[9] P. Tzvetkov, N. Petrova, D. Kovacheva, J. Alloys Comp. 485 (2009) 862–866.
[10] I.V. Nikolaev, H. D'Hondt, A.M. Abakumov, J. Hadermann, A.M. Balagurov, I.A. Bobrikov, D.V. Sheptyakov, V.Yu. Pomjakushin, K.V. Pokholok, D.S. Filimonov, G. Van Tendeloo, E.V. Antipov, Phys. Rev. B 78 (2008) 024426.
[11] J. Hadermann, A.M. Abakumov, T. Perkisas, H. D'Hondt, H. Tan, J. Verbeeck, V. Filonenko, E.V. Antipov, G. Van Tendeloo, J. Solid State Chem. 183 (2010) 2190–2195.
[12] V. Petricek, M. Dusek, The Crystallographic Computing System JANA2000, Institute of Physics, Praha, Czech Republic, 2000.
[13] C. Koch, Ph.D. Thesis, Arizona State University, 2002.
[14] S.A. Bruggemann, Y.A. Artzybashev, S.V. Orlov, ((UNIVEM) Version 4.5 (1990–1993).
[15] I.D. Brown, D. Altermatt, Acta Cryst. B41 (1985) 244.
[16] I.D. Brown, A. Dabkowski, A. McCleary, Acta Cryst. B53 (1997) 750.
[17] G.W. Watson, S.C. Parker, J. Phys. Chem. B 103 (1999) 1258.
[18] G.W. Watson, S.C. Parker, G. Kresse, Phys. Rev. B 59 (1999) 8481.
[19] F. Menil, J. Phys. Chem. Solids 46 (1985) 763–789.
[20] I.S. Liubutin, T.V. Dmitrieva, A.S. Stepin, JETP Letters 115 (1999) 1070–1084.
[21] T.C. Gibb, A.J. Herod, N. Peng, J. Mater. Chem. 5 (1995) 91–96.
[22] O. Helgason, F. Berry, T. Moyo, X. Ren, Hyperfine Interact. 168 (2006) 1165–1169.